JPhys Materials

PURPOSE-LED PUBLISHING™

PAPER • OPEN ACCESS

Tailoring optical and thermal properties in rare-earth doped MoS_2 for device applications

To cite this article: Geeta Sharma *et al* 2026 *J. Phys. Mater.* **9** 025002

View the article online for updates and enhancements.

You may also like

- Evaluation of electron–phonon coupling strength and average phonon energy in MoS_2 thin film
Umidakhon Rayimjonova, Daisuki Kawai, Ryu Hasunuma et al.
- Large Area Growth of MoS_2 By Chemical Vapour Deposition
Emma Coleman, Scott Monaghan, Farzan Gity et al.
- *(Invited)* Overview of ALD Synthesized MoS_2 Thin Films
Helmut Baumgart, Min Zeng, Kai Zhang et al.

This content was downloaded from IP address 81.102.248.232 on 15/05/2026 at 13:47

IOP Publishing J. Phys. Mater. 9 (2026) 025002 https://doi.org/10.1088/2515-7639/ae409f

Journal of Physics: Materials

Check for updates

OPEN ACCESS

RECEIVED
29 April 2025

REVISED
8 January 2026

ACCEPTED FOR PUBLICATION
2 February 2026

PUBLISHED
17 February 2026

Original content from this work may be used under the terms of the Creative Commons Attribution 4.0 licence.

Any further distribution of this work must maintain attribution to the author(s) and the title of the work, journal citation and DOI.

PAPER

Tailoring optical and thermal properties in rare-earth doped MoS_2 for device applications

Geeta Sharma[1,*], **Eric Kumi Barimah**[1], **Chun Wang**[2], **Sarathkumar Loganathan**[1], **Andrew Scott**[1] and **Animesh Jha**[1]

[1] School of Chemical and Process Engineering, University of Leeds, Leeds, United Kingdom
[2] School of Mechanical Engineering, University of Leeds, Leeds, United Kingdom
[*] Author to whom any correspondence should be addressed.

E-mail: g.sharma@leeds.ac.uk

Keywords: rare-earth doping, 2D materials, transition metal dichalcogenides, cross-sectional TEM, spectroscopy

Supplementary material for this article is available online

Abstract

The work presents a detailed account of the structural, optical, and thermal properties of ytterbium-doped molybdenum disulfide (MoS_2:Yb^{3+}) thin films. The thin films were grown by femtosecond pulsed laser deposition technique. The thickness of the films was varied from 1–10 nm. The structural characterizations were performed using x-ray photoelectron spectroscopy, transmission electron microscopy, and Raman spectroscopy which reveal an enhancement of crystallinity and strain relaxation with increasing thickness. Temperature-dependent Raman spectroscopy indicates Yb^{3+}-induced phonon anharmonicity, reflecting in-plane strain compensation and enhanced interlayer charge transfer. It is found that Yb^{3+} doping reduces thermal conductivity compared to pristine MoS_2, due to increased phonon scattering. The findings confirm the direct relationship between the changes in the lattice induced by the dopants and the phonon transport. This points to the fact that doping with rare earths together with control of thickness can modify the thermal and structural properties of two-dimensional materials. This work demonstrates co-engineering strategy of defects and thickness provides a scalable pathway that can be used for the production of functional MoS_2-based materials for next-generation applications of optoelectronics and heat management.

1. Introduction

Two-dimensional (2D) materials such as graphene, molybdenum disulphide (MoS_2), hexagonal boron nitride (h-BN) and tungsten disulfide (WS_2), exhibit high carrier mobility (~10000 cm^2 $(V{\cdot}s)^{-1}$ for graphene), tuneable bandgaps (~1.8 eV for monolayer MoS_2), strong light-matter interactions, exceptional mechanical strength (~1 TPa for graphene) and high thermal conductivity (~300–500 W $(m{\cdot}K)^{-1}$ for graphene) [1–3]. These characteristics make them of special interest to quantum technologies, energy and electronics [4]. Among these materials, MoS_2, a member of the transition metal dichalcogenide (TMD) family has garnered significant attention due to its unique electronic and optical properties, which vary dramatically with dimensionality and surface structure [4, 5]. The monolayer structure of MoS_2 has a direct bandgap of ~1.8 eV, is therefore extremely promising for use in photodetectors, LEDs, and solar cells [6, 7]. Nevertheless, practical use of MoS_2 in devices usually requires modification of its properties to optimize functionality and facilitate integration in real-world applications.

To tailor the electrical and optical properties of MoS_2, doping is a useful technique that involves adding foreign atoms or ions [8]. The doping of rare-earth elements such as Yb^{3+} with MoS_2 was posited to gain significantly in performance. In particular, the Yb^{3+} ion is well noted due to its large optical absorption and emission around 980 nm in the NIR region associated with the transition from $^2F_{5/2}$ to $^2F_{7/2}$ [9]. Yb^{3+} doping introduces localized energy states in the bandgap of MoS_2 to facilitate energy

© 2026 The Author(s). Published by IOP Publishing Ltd

transfer processes to increase PL and widen its optoelectronic use [8]. Yb^{3+} ions have been demonstrated to emit sharp NIR PL peaks around 975–1020 nm wavelengths to drive improvements in photodetectors, NIR sources, and optoelectronics [10]. Besides doping, film thickness of MoS_2 plays a crucial role in properties [6]. In bulk MoS_2, the material exhibits an indirect band gap of ∼1.2 eV, which transitions to a direct band gap of ∼1.8 eV when reduced to a monolayer [11].

The present study investigates the influence of electron–phonon coupling with thickness in ytterbium (Yb^{3+})-doped MoS_2 thin films. Even though such interactions are central to thermal transport and optoelectronic properties, tuning through rare-earth doping and film thickness is poorly understood. Temperature-dependent Raman spectroscopy is a robust probe and shifts in E^1_{2g} and A_{ig} phonon modes are signatures of lattice anharmonicity and doping-induced strain effects. While dynamics of monolayer MoS_2 have been previously investigated [12] the dual impact of Yb^{3+} doping and thickness on phonon behavior remains under explored [13–16]. To address this, the present work investigates electron–phonon interactions and the concomitant structural and optical modifications across a well-defined thickness gradient 1–10 nm of Yb^{3+} doped MoS_2. The methodology is centered on exploiting femtosecond pulsed laser deposition (fs-PLD) to achieve precise incorporation of Yb^{3+} ions, which introduce significant local strain and distinct electronic states. It is demonstrated that the effect of these Yb^{3+} induced phonon scattering centers is profoundly modulated by film thickness, thereby establishing a 2D parameter space for material engineering. Defect-thickness co-engineering is an active and controllable method for tuning thermal and optoelectronic performance, thus providing a basic framework and expanding the conventional means of characterization. The knowledge gained can be directly transferred to the MoS_2 technology of the future, including, ultra-fast optoelectronics and integrated circuit thermal management, where exceptional charge and heat transfer control will be required. The present research employs various characterization techniques including x-ray photoelectron spectroscopy (XPS), PL, Raman spectroscopy, cross-section transmission electron microscopy (TEM), and UV–vis spectroscopy to probe Yb^{3+} ion incorporation, phonon dynamics, and photoluminescence characteristics. The insights obtained from these techniques are very important for improving MoS_2-based devices such as photodetectors, LEDs, and thermoelectric generators.

2. Experimental and methodology section

2.1. Fabrication of thin films

The undoped and Yb-doped MoS_2 thin films were deposited on fused quartz (SiO_2) substrates using the fs-PLD technique. Before deposition, the substrates were cleaned with acetone, isopropyl alcohol, and distilled water sequentially using an ultrasonic bath. The substrates were dried and baked under vacuum inside the deposition chamber. A turbo-molecular pumping system was used to maintain a base pressure below 1×10^{-6} Torr in the chamber.

A Ti:sapphire laser operating at a wavelength of 800 nm with a pulse duration of 100 fs and a repetition rate of 1 kHz was used for the deposition. The pulse energy was ∼12 μJ, corresponding to pulse energy density of ∼4.88 J cm^{-2} at the target, and focused to a ∼25 μm spot. To ensure uniform ablation and minimize localized heating the target was continuously rotated.

The target material was prepared by pressing MoS_2 pellets and 3% Yb^{3+} doped MoS_2 powder synthesized via hydrothermal process [17] (details of the process are discussed in the supplementary section SS1). During deposition, the substrates were maintained at 500 °C on a resistively heated substrate holder positioned 50 mm away from the target. The deposited films were left to cool at a rate of about 5 °C min^{-1} to room temperature.

The thickness of the MoS_2:Yb^{3+} films was adjusted by varying the deposition time (40, 120, 150, and 240 s). A schematic representation of the fs-PLD setup, showing the laser beam path, target, ablation plume, and heated substrate geometry, is provided in figure 1. The various characterizations of the deposited films are discussed in the following sections.

2.2. Characterization of films

The Renishaw Raman inVia Microscope (laser excitation at 514 nm) was used to characterize the MoS_2 thin films. A 50x microscope objective and 0.8 NA was used. The gratings used in Raman spectroscopy had a spectral resolution of greater than 1 cm^{-1} and a step size of 3–4 μm. To prevent laser-induced film deterioration, the laser power was maintained below 1 mW. Internal silicon (Si) was used to calibrate the spectral position. The schematic of the Raman spectrometer is shown in the supplementary figure S1.

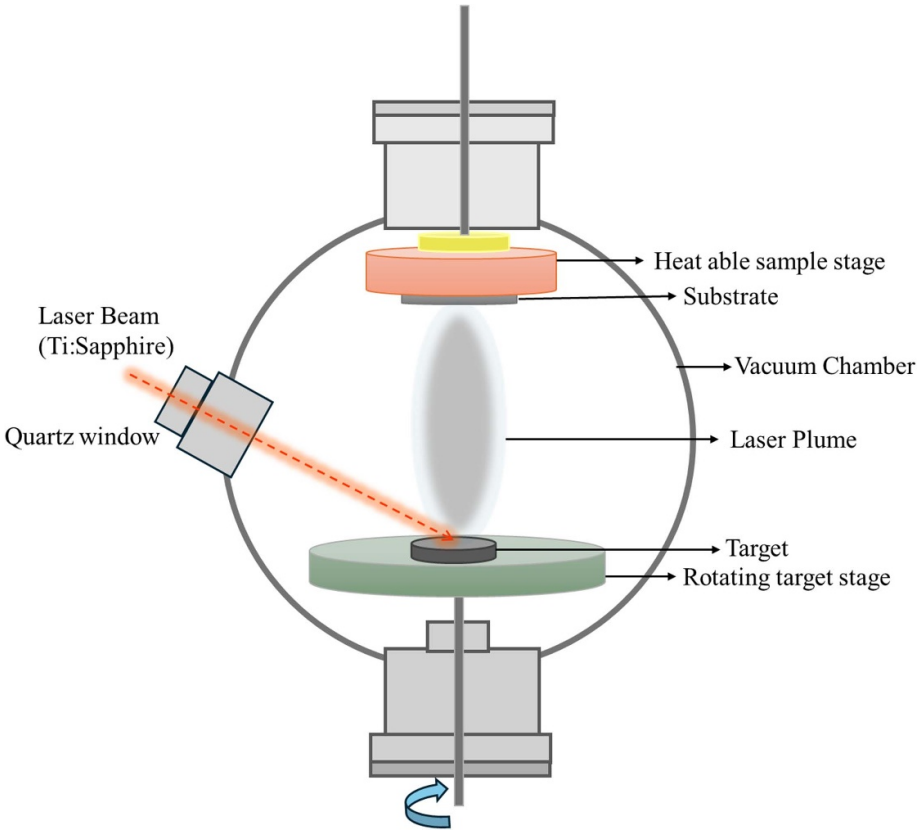

Figure 1. Schematic representation of the fs-PLD system used to grow MoS_2 thin films. The diagram shows, material is deposited onto a heated substrate by an ablation plume created when the laser beam is focused onto a rotating target.

The samples were heated (5 °C s^{-1}) for Raman measurement by placing on a heating plate which can be accommodated in the Raman spectrometer. The surface temperature of the film was measured using a K-type thermocouple (Thermosense, UK) with a resolution of 0.24 °C.

The temperature dependence of the Raman peak positions was analyzed using an empirical relation to account for phonon anharmonicity [18, 19] (equation (1)):

$$\omega(T) = \omega_0 + \alpha(T - T_0) + \beta(T - T_0)^2 \quad (T_0 = 20^{\circ}\mathrm{C}) \tag{1}$$

where the coefficients α (linear) and β (quadratic) quantify phonon anharmonicity.

Cross-section TEM was conducted using an FEI Tecnai FT20 field emission microscope at 200 kV operating acceleration voltage. Sample preparation was done within a focused ion beam system (FEI Helios G4 UX). The surface of the film was first shielded with a platinum protection layer by electron- and ion-beam-induced deposition to prevent damage by ions during milling. Thin lamellae ($\sim$100 nm thick) were then picked up and transferred to a TEM grid using a micromanipulator and thinned to electron transparency at low ion beam currents ($\leqslant$50 pA) while minimizing amorphous damage. Abating sample charging and beam damage was a critical part of obtaining high-resolution images; this was done by applying a relatively low beam current and brief imaging exposure times.

For optical absorption measurements, a Perkin-Elmer UV–Vis–NIR spectrophotometer equipped with a 60 mm integrating sphere was employed to record the excitonic absorption bands. An integrating sphere is necessary for the measurement of thin films on substrates because it gathers both the directly transmitted light and the diffusely scattered light, enabling accurate absorption not confused by scattering losses. The baseline correction was performed with an uncoated substrate as reference to compensate for substrate absorption. No particular preparation of the samples was required other than ensuring that they were clean and well positioned at the entrance port of the integrating sphere. The schematic of the UV–Vis–NIR spectrophotometer is shown in the supplementary figure S2.

An XR50 x-ray monochromatic AlK_α (1486.5 eV) high intensity SPECS system and a PHOBIOS hemispherical electron analyzer with a pass energy of 30 eV and a vacuum of 10^{-10} Torr were used to get XPS spectra. The maintenance of ultra-high vacuum ($\leqslant 10^{-9}$ Torr) was necessary to avoid the contamination of the surface during the measurement. In addition, since the films were deposited on

non-conductive fused quartz substrates, a low-energy flood gun was applied to counteract the charging effects and to guarantee the accurate binding energy calibration. Energy calibration was referenced to the adventitious *C*1*s* peak at 284.6 eV. Spectral deconvolution was performed using Casa XPS software with a Shirley background subtraction. The core-level peaks (e.g., Mo 3*d*, S 2*p*, Yb 4*d*) were fitted with a combination of Gaussian–Lorentzian line shapes (GL), specifically a 70% Gaussian/30% Lorentzian (GL 70/30) product function, which is standard for XPS analysis. The error on the peak position was given by the standard error of the fit algorithm (±0.1 eV). Full width at half maximum (FWHM) for peaks of the same chemical state was restricted to be the same in the fitting procedure.

X-ray reflectivity (XRR) data was collected using the EMPYREAN diffractometer. The sample was precisely positioned and aligned using a 5-axis cradle. The apparatus has a Theta/Theta goniometer with a minimum step size of 0.0001° for 2 Theta and Omega to enable the collection of high-resolution data. The 240 mm Chi-Phi-*X*–*Y*–*Z* sample stage features a minimum of 0.01° for Chi and Phi, 0.01 mm for *X* and *Y*, and 0.001 mm for *Z* for accurate measurement correction. It is possible to fine-tune the orientation of the sample. Surface roughness has a huge impact on the precision of thickness and density fitting. The films were required to be very smooth (roughness <1–2 nm) and flat because too much roughness would reduce the contrast of the interference fringes and make the modeling more difficult.

The modeling the x-ray reflectivity (XRR) data was done to determine the thickness of the deposited films. The fringes observed in form of oscillating pattern in the XRR curve (figure 2) results from the constructive and destructive interference of x-rays reflected from the air-film and film-substrate interfaces. To the film thickness, d is inversely proportional to the period of these oscillations, $\Delta(2\theta)$, following the relationship $d \approx \lambda/(2\ \Delta(2\theta))$, where λ is the x-ray wavelength. GenX software was utilized to fit the experimental data. The best match between the simulated and measured reflectivity curve, was obtained by iterative refinement of parameters for thickness, density, and surface roughness. The goodness-of-fit was measured by the figure of merit (FOM) value, and the estimated uncertainty in the thickness values is ±0.2 nm.

X-ray reflectivity or XRR measurements were performed to get the thickness, density, and interface roughness of the thin films. The GenX software, applies a differential evolution algorithm for parameter optimization. The fitting was done using the Parratt recursive formalism, which simulates the x-ray reflectivity from multilayer thin films by considering the electron density contrasts at each interface. The Nevot–Croce correction was used to include the surface and interface roughness effects in the mo this correction adjusts the Fresnel reflection coefficients to consider Gaussian interface roughness. By iteration, the best parameters were retrieved through the process of minimizing the difference between the experimental and theoretical reflectivity curves. The relative percentage error (RPE) between the fitted model and experimental data was maximum 3.5%, which reflects excellent agreement and hence, trustworthy structural parameter extraction,

$$\mathrm{RPE}_{\max} = \max\left(\frac{|\, I_{\mathrm{exp}} - I_{\mathrm{fit}}\,|}{I_{\mathrm{exp}}} \times 100\%\right)$$

where I_{exp} and I_{fit} represent the experimental and fitted intensities, respectively.

Using a Bruker Dimension Icon atomic force microscopy (AFM) in contact mode, surface morphology was examined to look at the topography of films and surface roughness. For topographical measurements with great spatial resolution, an NM-TC AFM tip with a tip radius of less than 20 nm was employed. The necessary feature analysis was used to modify the scan size and resolution. The vertical resolution offered by the AFM system is better than 1 nm. The scanning force was carefully regulated to the lowest possible level to reduce any potential tip-induced changes. The scan angle was 90° and the tip velocity was 9.96 μm s^{-1}.

3. Results and discussion

3.1. Thin film thicknesses and cross-section layered structure

The thicknesses of Yb^{3+}doped MoS_2 films deposited for varying durations were analyzed using X-ray reflectivity (XRR) measurements, as shown in figure 2. The film thickness, estimated by fitting the XRR data, are ∼ 1.8, 2.8, 4.3, and 10.2 nm for samples deposited for 40 s, 120 s, 150 s and 240 s respectively. The thickness of the films was obtained by fitting the XRR profiles using the standard Parratt formalism implemented in GenX software. The fits were optimized by minimizing the FOM to obtain the best agreement between experimental and simulated data.

Cross-sectional analysis of the films was performed using TEM. Figures 3(a) and (b) present cross-sectional TEM images of the films deposited for the maximum (240 s) and minimum (40 s) durations,

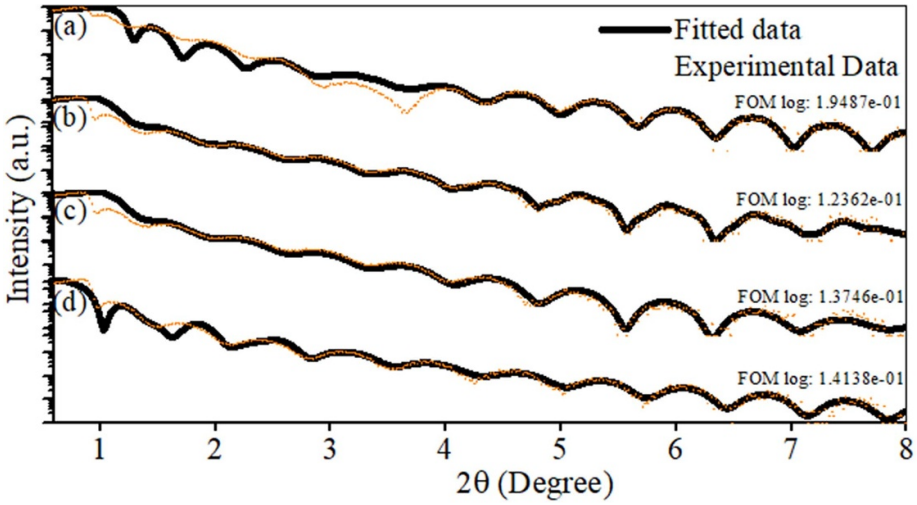

Figure 2. X-ray reflectivity (XRR) measurements of Yb^{3+} doped MoS_2 films deposited for (a) 240 s, (b) 150 s, (c) 120 s, and (d) 40 s. The experimental data were fitted using GenX software to determine the thicknesses of the films.

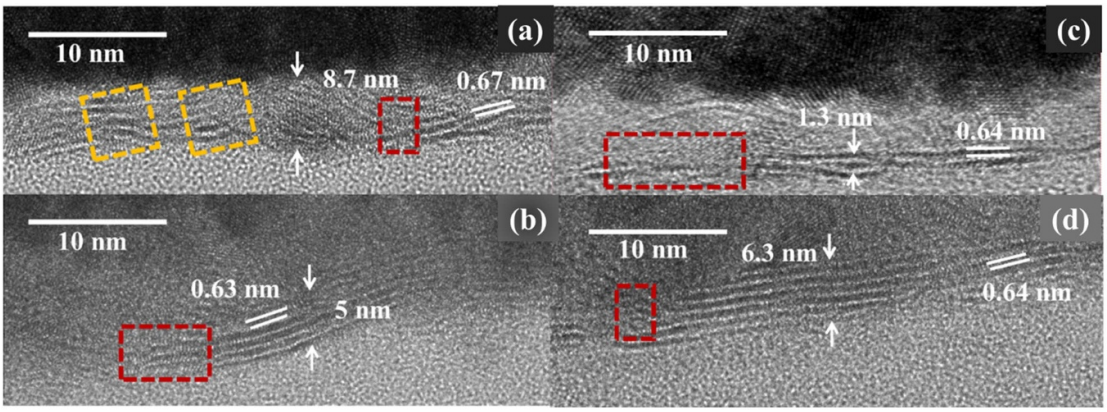

Figure 3. TEM images of MoS_2: Yb films deposited for (a) 250 s, (b) 150 s, and (c) 40 s, together with (d) an undoped MoS_2 film deposited for 150 s. The corresponding film thicknesses are approximately 8.7, 1.3, 5, and 6.3 nm, respectively. White arrows denote the overall film thickness, while white double arrows indicate the interlayer spacings (0.63–0.67 nm), consistent with the characteristic MoS_2 d-spacing. Regions of structural variation are illustrated with dashed boxes: yellow boxes indicate stacking irregularities, while red boxes indicate more diffused areas. In general, diffused appearance is a characteristic of thinner films, while localized stacking irregularities and interlayer variations are observed in thicker films. The undoped film have relatively uniform structure, which suggests that the Yb ion doping along with film thickness is the factor contributing to the local structural inhomogeneities.

respectively. The thickest film reveals a thickness of ∼8.7 nm, while the thinnest film shows a thickness of ∼1.3 nm. The thickest and the thinnest films show the relative error of approximately 14.7% and 27.8% respectively between XRR and TEM results. The larger difference observed for the ultrathin film may arise from interface roughness and limited TEM contrast at the film–substrate boundary for thin samples. Overall, the consistent trend between both techniques confirms the precision of the film thickness control.

Figures 3(a)–(d) shows TEM images of MoS_2:Yb ion doped films deposited for different times (250 s, 150 s, and 40 s) and an undoped MoS_2 film deposited for 150 s for comparison. The measured thicknesses of the Yb ion-doped films are approximately 8.7 nm, 5 nm and 1.3 nm for 250 s, 150 s, and 40 s respectively. The undoped film (deposited for 150 s) has a thickness of approximately 6.3 nm. The interlayer spacings, indicated in the images, are around 0.67 nm for the thicker films and 0.63–0.64 nm for the thinner films, values consistent with the characteristic d-spacing of MoS_2 [20]. The slight variations in spacing may be due to thickness-dependent growth dynamics [20]. The microstructural differences between the films are annotated in the figures 3(a)–(d). Thinner Yb ion-doped films, although generally continuous, appear more diffused, whereas the thicker doped films exhibit areas where stacking irregularities and local interlayer spacing variations are observed. Whereas the undoped film (figure 3(d)) appears comparatively more uniform, with fewer visible irregularities. These observations suggest that

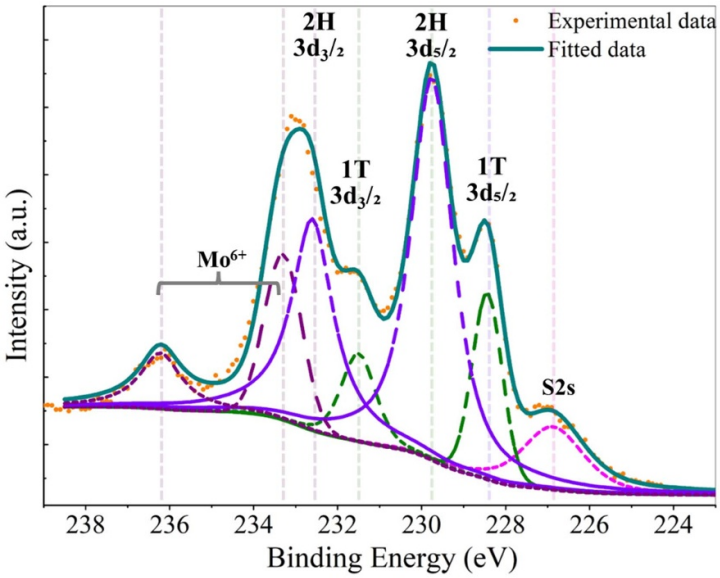

Figure 4. XPS spectrum of the Yb^{3+} doped MoS_2 films deposited for 240 s showing Mo3*d* region for deconvoluted profile with seven peaks, indicating the presence of a mixed phase in the thin films. The XPS spectra were analyzed using a Shirley background and Voigt line shapes, with and area ratios allowed to vary only within the standard literature values for Mo core levels. The goodness of fit, indicated by the values for χ^2, was found to be 1.60.

Yb ion incorporation, together with thickness, impact structural uniformity. The optical and electronic properties of MoS_2 based devices can be greatly influenced by such subtle changes in microstructure [21].

The EDAX analysis (supplementary figure S3) verifies the existence of molybdenum and sulphur, while the elemental mapping reveals an even distribution of the two elements throughout the surface of the film. The AFM analysis was carried out to investigate the impact of deposition time and Yb ion doping on the surface morphology of MoS_2 thin films. The results show that surface roughness increases with deposition time, and that Yb-doped films are rougher than undoped films deposited under identical conditions. A detailed comparative analysis with AFM images is provided in the supplementary information SS2 (figure S4, in the supplementary section).

3.2. Phase composition and electronic structure

The XPS analysis offers critical information about phase composition, oxidation states, and bonding environments. The XPS survey spectra of pristine and Yb^{3+} doped MoS_2 films (240 s) are presented in figure S8 in the supplementary section. The emergence of Yb peaks in the doped sample is a clear sign of the Yb ion doping with no detectable impurities. The XPS spectrum of the Mo3*d* region for MoS_2 doped with Yb ion films deposited for 240 s is shown in figure 4, revealing a deconvoluted spectrum comprising seven peaks. The 3*d* doublet peaks associated with the metallic 1 T phase are observed at 228.4 eV for $3d_{5/2}$ and 231.5 eV for $3d_{3/2}$, while the semiconducting 2H phase exhibits peaks at 229.6 eV ($3d_{5/2}$) and 232.7 eV ($3d_{3/2}$). Additionally, peaks at 233.3 eV and 236.3 eV are attributed to the oxidation states of molybdenum (Mo^{6+}), indicating some degree of oxidation within the films, which can introduce defect states or trap levels influencing the optical properties. The peak at 226.8 eV corresponds to contributions from S2*s* electrons, further elucidating the sulphur environment around the molybdenum atoms [22, 23].

XPS S2*p* (figure S6(a) in the supplementary section) pattern of MoS_2 shows distinguishable peaks indicating the 2 H and 1 T phases, which are of interest to understand electronic structure and sulphur bonding condition. In case of 2 H phase, the S $2p_{3/2}$ and S $2p_{1/2}$ peaks are observed at 162.8 eV and 164.0 eV, respectively, whereas for the 1 T phase, these peaks appear at lower binding energies of 162.3 eV and 163.6 eV [22]. These variations in binding energies are due to variations in the local electronic sulphur environment brought about by the difference in coordination geometries of the two phases of MoS_2: trigonal prismatic in the 2 H semiconducting phase and octahedral in the 1 T metallic phase. Confirmation of the existence of Yb ion in the Yb^{3+} oxidation state comes from the Yb4*d* spectrum (figure S6(b) in the supplementary section). The Yb4$d_{5/2}$ peak is observed at 185.8 $\pm$ 0.5 eV, which is consistent with the Yb ion being in the 3+ oxidation state with a sulphur coordination shell[22, 24]. Yb^{3+} doping may cause redistribution of charge, which alters the electronic environment of S and

Mo atoms, as suggested from the alteration of the Mo3*d* valence band spectrum upon Yb^{3+} doping (The details are discussed in supplementary section SS3; figure S7 in the supplementary section).

In addition, Yb^{3+} incorporation into the MoS_2 lattice may cause creation of new electronic states or strain effects, both of which can be responsible for the shifts in binding energy observed. Herein, the detected shift to higher binding energies in the XPS *Mo3d* core-level spectra (figure S5, supplementary information) contrasts with the observation of shifts toward lower binding energies of MoS_2 films deposited under an argon atmosphere. This difference is due to the deposition atmosphere. Argon constitutes a mildly reducing atmosphere and thus considered to promote the transfer of electrons from Yb atoms to the MoS_2 lattice and lower binding energies. In contrast, under the vacuum deposition method, the reducing effect of argon is absent. Hence, the incorporation of Yb^{3+} ions result in slight electron depletion and local lattice distortions, ultimately leading to an increase in the binding energies reported here.

The XPS spectra were fitted with a Shirley background and Voigt line shapes, with spin–orbit splitting and area ratios allowed to vary only within the standard literature values for Mo, S, and Yb core levels. The values for χ^2 indicating goodness of fit were found to be 1.60 in the Mo 3*d*, 2.08 in the S 2*p* and 1.70 in the Yb 4*d* region, indicating a good agreement between the experimental and the fitted spectra. Binding energies and peak separations and relative intensities upon deconvolution are consistent with literature values, which confirm the trustworthiness of the fitting procedure. The XPS data shown for the 240 s sample are representative of all thicknesses since chemical states remain consistent, and Yb^{3+} incorporation is kept constant across the series due to identical deposition conditions.

3.3. Absorption spectra and excitonic transitions

Figure 5(i) shows the absorption spectra of MoS_2: Yb^{3+} films deposited for various durations: (a) 240 s, (b) 150 s, (c) 120 s, and (d) 40 s. The presence of direct excitonic transitions, designated as 'A' and 'B,' are evident from the slight increase in absorbance around 670 nm and 615 nm. These excitonic transitions take place in the Brillouin zone *K* point between the valence band split maxima and the conduction band minimum [11]. Around 440 nm and 290 nm, there is wide increase in absorbance that indicate the 'C' and 'D' transitions, which are linked to Van Hove singularities in the electronic density of states of multilayer MoS_2 [6]. Figure 5(i) shows that background absorption increases with the thickness of the MoS_2 films. The formation of grain boundaries and higher density of point defects might be leading to the increase in background absorption with thickness. These defects create mid-gap states that act as absorption centers [25]. This is consistent with the charge difference between Yb^{3+} and $Mo^{4}+$ ions, which introduces donor levels into the MoS_2 lattice [4, 11]. These types of defects, along with their points and interfaces, can still exist where the material has been locally crystallized to a high degree. Also, this can be inferred due to the narrowing of Raman peaks observed in thicker films (section 3.4). It is clear from the valence band spectra that due to Yb^{3+} doping there is increased density of states near the valence band maximum (details of valence band spectroscopy analysis is shown in figure S7 in supplementary section). Additionally, the Yb^{3+} ions octahedral crystal field distortion breaks the structural continuity of the formed 2D films, which may be a factor in Rayleigh-scale scattering [26, 27].

The absorption intensity demonstrates a non-linear dependence on film thickness, with a more pronounced increase observed between 1.8 nm and 2.8 nm compared to between 2.8 nm and 4.3 nm, despite comparable absolute thickness differences. One of the reasons for such a behavior is the emergence of a critical thickness range of about 2–4 layers where the quantum confinement effects quickly lessen and the interlayer screening effect becomes more significant [28]. The increase in absorption is more prominent in the thinner film limiting the major modification in the electronic density of states when the system switches from few-layer to multilayer phase, which is in line with the documented thickness-related optical properties in 2D TMDs. Specifically, the absorption saturation beyond ∼3 layers has been attributed to reduced quantum confinement and enhanced dielectric screening effects [29].

3.4. Raman spectroscopy and structural insights

The Raman spectra of MoS_2:Yb^{3+} (figure 5(ii) and supplementary figure S9) show the presence of both semiconducting 2 H and metallic 1 T phases, which are identical to the phases revealed by the XPS results. The main contributors to the spectra are the modes related to the 2 H phase: the in-plane E^1_{2g} peak and the out-of-plane A_{1g} peak. The lower frequency regions present the characteristic J_2 (∼230 cm^{-1}) and J_3 (∼330 cm^{-1}) modes of the 1 T phase [30, 31]. The analysis primarily focuses entirely on the E^1_{2g} and A_{1g} modes, because these two phonon modes as they reveal the clear signature of thickness-dependent phonon behavior and the interlayer coupling.

Figure 5(ii), and table 1 shows the systematic variations in the Raman spectra upon changes in the thickness. It is observed that a definite trend is being set by the increase in thickness ranges from 1.8 nm to 10.2 nm for the E^1_{2g} mode to move down from 379.0 cm^{-1} to 376.4 cm^{-1}. Concurrently,

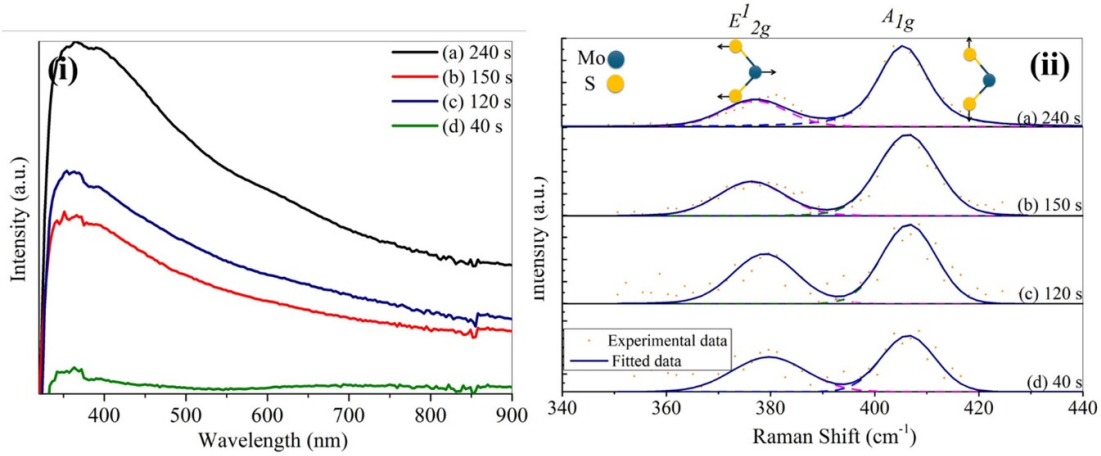

Figure 5. (i) UV–visible absorption spectra of MoS_2: Yb^{3+} films deposited for durations of (a) 240 s, (b) 150 s, (c) 120 s, and (d) 40 s, showing prominent excitonic bands at 615 nm and 670 nm; (ii) Raman spectra of MoS_2: Yb^{3+} doped films for deposition times of (a) 240 s, (b) 150 s, and (c) 120 s, highlighting characteristic vibrational modes of MoS_2. The experimental data were accurately represented by all Raman spectra being fitted with a sum of Voigt functions. This was also supported by reduced chi-squared (χ^2) values of 1.1, 1.5, 1.7, and 1.8 for the 240 s, 150 s, 120 s, and 40 s deposition samples, respectively.

Table 1. Raman peak positions (E^1_{2g} and A_{1g}), full width at half maximum (FWHM) of E^1_{2g}, and frequency difference (ΔF) for MoS_2: Yb^{3+} films deposited at varying durations (240 s, 150 s, 120 s and 40 s), illustrating the influence of deposition time on vibrational modes and structural properties.

Deposition time (s)	E^1_{2g} (cm^{-1})	A_{1g} (cm^{-1})	FWHM of E^1_{2g}	ΔF (cm^{-1})
240	376.4 ± 0.3	407.2 ± 0.1	11 ± 1	30.8 ± 0.6
150	378.6 ± 0.1	406.7 ± 0.2	14 ± 1	28.1 ± 0.8
120	378.9 ± 0.2	406.5 ± 0.3	34 ± 2	27.6 ± 0.5
40	379.0 ± 0.3	406.2 ± 0.2	37 ± 3	27.2 ± 0.6

the A_{1g} mode shifts from 406.2 cm^{-1} up to 407.2 cm^{-1}. This opposite shifts in the two bands leads to increase in the peak separation ($\Delta\omega$) from 27.2 cm^{-1}–30.8 cm^{-1}. This is a clear indicator of transforming from few layers to multilayer system. The E^1_{2g} mode downshift is attributed to the combination of the increased interlayer interactions and the lattice strain relaxation as the number of layers add. The A_{1g} mode upshift is due to the variation of MoS_2 mechanical properties with the thickness due to the significantly enhanced interlayer coupling [32].

The thicker films exhibit a significant decrease in the FWHM of the E^1_{2g} mode (from 37 ± 3 cm^{-1} for the 1.8 nm film to 11 ± 1 cm^{-1} for the 10.2 nm film). This might be due to improved short-range crystalline order and reduced phonon confinement effects, which favor more coherent phonon modes [33, 34].

The phenomenon of reduced linewidths of the Raman peaks is in line with the increased film thickness leading to the relaxation of in-plane strain and improvement of crystallographic coherence. Interlayer coupling in MoS_2 films may also affect their vibrational modes by changing the phonon dispersion [35]. All Raman spectra were fitted with a sum of Voigt functions, yielding excellent agreement with the experimental data, as evidenced by reduced chi-squared (χ^2) values of 1.1, 1.5, 1.7 and1.8 for the 240 s, 150 s, 120 s and 40 s deposition samples, respectively.

3.5. Photoluminescence and decay characteristics

Figures 6(i) and (ii) present the room-temperature PL and lifetime measurements of MoS_2: Yb^{3+} films, obtained using a 976 nm laser diode as the excitation source. The PL decay characteristics of the thin film is shown in figure S10 in the supplementary section. Photoluminescence decay curves (supplementary figure S10) were analyzed by fitting with a single-exponential decay function, equation (2)

$$I(t) = I_0 \exp\left(\frac{t}{\tau}\right) + C \tag{2}$$

where $I(t)$ is the PL intensity at time t, I_0 is the initial intensity, and τ is the lifetime and C is a constant accounting for background noise. The goodness of the fit was indicated by the coefficient of

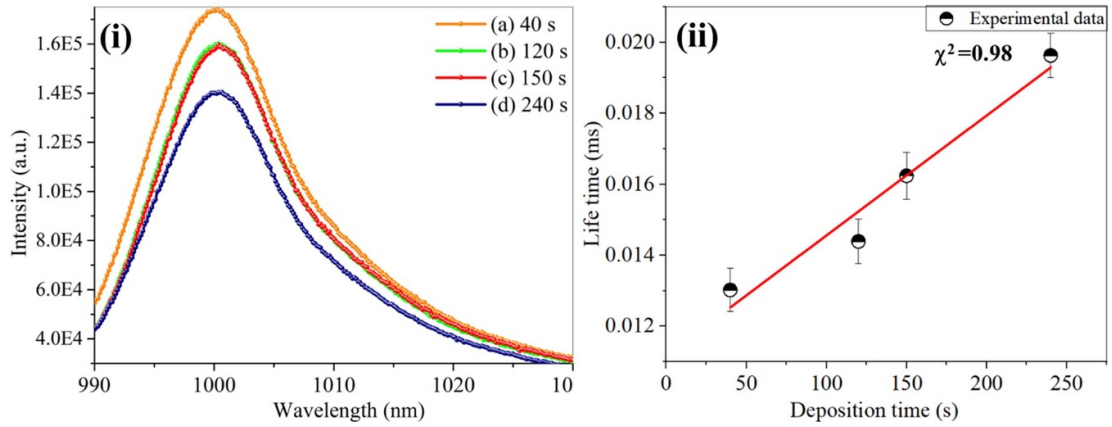

Figure 6. (i) Room-temperature PL spectra of MoS_2:Yb^{3+} films deposited for different durations: (a) 40 s, (b) 120 s, (c) 150 s, and (d) 240 s, showing emission in the near-infrared region around 1000 nm; (ii) lifetime measurements of MoS_2:Yb^{3+} films as a function of deposition time, indicating an increase in lifetime with longer deposition durations.

determination (R^2) which was close to 0.98 for all the samples. The error in the lifetime values represents the standard deviation from fitting multiple measurements on different sample areas.

The Yb^{3+} doped MoS_2 film room-temperature PL is in good agreement with that of the PL properties of Yb^{3+} doped glass materials [36, 37]. Despite the small volume of the film relative to bulk material, and therefore the respective impact of inhomogeneous broadening on PL line shape, the FWHM of the optical transition ($^2F_{5/2} \rightarrow {}^2F_{7/2}$) is less than 12 nm with an emission maximum at 1002 nm [22]. In bulk materials, this transition is comparatively wider (70–80 nm FWHM). The thin film constrained dimensions seem to be the cause of this FWHM narrowing in comparison to the wider 70–80 nm seen in bulk materials. Figure 6(i, ii) illustrates a distinct relationship between film thickness and PL characteristics. The thinner films (40 s deposition) have the shortest lifetime (∼0.012 ms), i.e., fast and efficient radiative recombination. This indicates that there are fewer defects and lower strain in the thinner films, enabling the excitons to recombine radiatively and thus stronger PL emission. It is believed that the longer lifetime of the PL in the thick layers (∼0.019 ms for the 10.2 nm film) is due to the higher density of defects, e.g. the stacking faults and grain boundaries seen in the TEM images (figure 3). Normally, the defects would facilitate the non-radiative recombination of carriers, however, they can in some cases be the trapping centers for excitons which would prolong the carrier lifetime by slowing down the recombination process. Increased lifetimes in thick films reflect lower recombination dynamics because of defect trapping and a more relaxed crystalline structure. The PL characteristics identified highlights the contribution of film thickness to radiative efficiency and recombination kinetics. The PL and lifetimes suggest that thin films, with greater PL intensity and shorter lifetimes, are suitable for optoelectronic devices such as LEDs and laser diodes, where rapid radiative recombination is preferred. Thick films, with lower PL intensity and longer lifetimes, would be better suited for photovoltaics and photodetectors, where slow recombination facilitates carrier collection. The recombination channels which are non-radiative in thicker films could have useful applications like thermal management, where dissipation of energy via heat is beneficial. PL tunability and thickness-dependent recombination dynamics facilitate engineering of MoS_2 devices for some functionalities to encompass efficient light generation through to energy harvesting and complex sensing systems.

At first sight, the observation of narrower Raman linewidths and longer PL lifetimes in thicker films seems to be contradictory, but this is due to different physical phenomena the mentioned techniques investigate. Raman spectroscopy is sensitive to short-range crystalline order and phonon confinement, which improves with thickness due to strain relaxation. On the other hand, the PL lifetime is governed by the density of defects such as stacking faults, which act as exciton traps that delay recombination. This interpretation agrees with the TEM analysis (figure 3), which shows that thicker films exhibit both well-defined layered structure (consistent with improved short-range order) and the presence of stacking faults (providing exciton trapping sites).

3.6. Analysis of thickness-dependent electron–phonon coupling in MoS_2: Yb^{3+} films

The charge transport and optoelectronic properties of 2D semiconductors are fundamentally affected by the electron–phonon interaction. A widely adopted phonon-induced linewidth model was used to study

Table 2. Calculated electron–phonon parameters for MoS_2:Yb^{3+} films of different thicknesses.

Thickness (nm)	Experimental Γ (300 K) (meV)	*A* (meV) from equation (4)	Calculated Γ0 (meV)
1.8	17.50 ± 0.10	10.9 ± 0.3	15.66 ± 0.10
2.8	16.94 ± 0.10	11.4 ± 0.2	15.01 ± 0.10
4.3	16.84 ± 0.10	12.2 ± 0.5	14.78 ± 0.12
10.2	16.73 ± 0.10	15.1 ± 0.6	14.18 ± 0.14

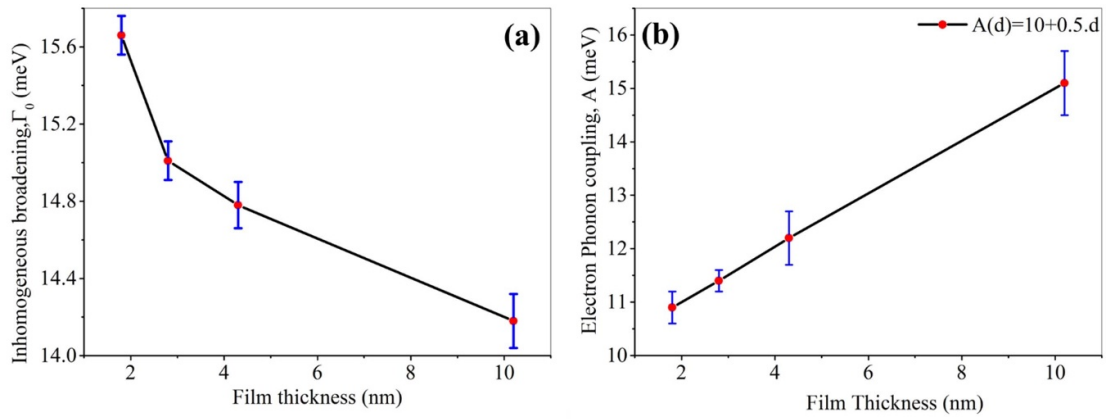

Figure 7. (a) Variation of inhomogeneous broadening Γ_0 with film thickness for MoS_2: Yb^{3+} films. The slight decrease with thickness reflects improved crystallinity. (b) Thickness-dependent electron–phonon coupling strength $A(d) = 10 + 0.5 \cdot d$.

the thickness-dependent electron–phonon parameters in MoS_2: Yb^{3+} films [38, 39] (equation (3))

$$\Gamma(T) = \Gamma_0 + \frac{A}{\exp\left(\frac{\hbar\omega_0}{k_B T}\right) - 1} \tag{3}$$

where $\Gamma(T)$ is the PL linewidth at temperature T, Γ_0 represents inhomogeneous broadening from static disorder, A is the electron–phonon coupling strength, $\hbar\omega_0 = 50$ meV is the phonon energy of MoS_2, and k_B is the Boltzmann constant (8.6173×10^{-2} meVK^{-1}).

Based on the physical principle of reduced quantum confinement in thicker films, it is proposed that the electron–phonon coupling strength increases linearly with thickness (as shown in equation (4)) [40, 41].

$$A(d) = 10 + 0.5 \cdot d(\text{meV, with } d \text{ in nm}). \tag{4}$$

Using the experimentally obtained room-temperature linewidths Γ (300 K) and electron phonon coupling strength, A in equation (3), the inhomogeneous broadening Γ_0 for each film thickness was calculated. The calculated parameters are summarized in table 2.

The room temperature value of $\exp\left(\frac{\hbar\omega_0}{k_B T}\right) - 1 \approx 5.92$, thus leading to an approximate phonon contribution of A/5.92. The obtained Γ_0 values reveal a steady decrease with sample thickness, from 15.66 meV (1.8 nm) to 14.18 meV (10.2 nm), which signifies better crystallinity in thicker films, in line with the Raman and TEM analyses (section 3.4). Whereas the electron phonon coupling strength, A, increases with thickness, indicating stronger phonon participation due to interlayer coupling and Yb^{3+}-induced lattice modulation.

The decline in Γ_0 signifies a more ordered lattice, and at the same time, the linear rise in A indicates that phonon coupling strength was enhanced with an increase in film thickness. These findings indicate that Yb^{3+} incorporation effectively tailors phonon transport and strain dynamics in 2D MoS_2 systems [8, 35, 38]. Figure 7(a) illustrates the thickness dependence of Γ_0, while figure 7(b) shows the variation of A with film thickness. These values are consistent with previously reported experimental measurements of MoS_2 thin films and other 2D materials [42–44]. To check how well the model corresponds to the experimental data the RPE was calculated using relationship, relative error (%) = $(\Gamma_{exp} - (\Gamma_0 + A/5.92))/\Gamma_{exp} \times 100$. The calculated errors are 0.00%, 0.12%, 0.06%, and 0.06% for 1.8 nm, 2.8 nm, 4.3 nm and 10.2 nm respectively. The process was considered reliable since all the relative error was less than 1.2%.

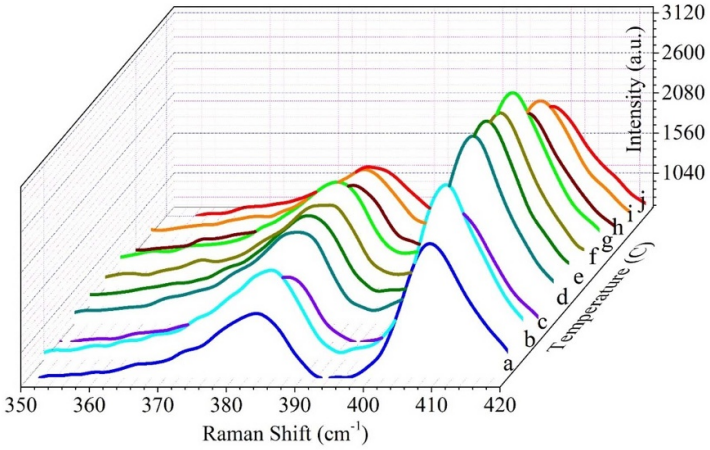

Figure 8. (a–j) Temperature-dependent Raman spectra of Yb^{3+}-doped MoS_2 thin film (deposition time: 240 s), recorded at 20 °C, 30 °C, 50 °C, 70 °C, 90 °C, 110 °C, 130 °C, 150 °C, 170 °C, and 200 °C, respectively. The spectra feature two characteristic peaks attributed to the in-plane E^1_{2g} mode and the out-of-plane A_{1g} mode of MoS_2. A consistent red shift in both modes is observed with increasing temperature (from (a) to (j)), indicating phonon softening due to thermal lattice expansion and anharmonic phonon–phonon interactions.

Table 3. Temperature-dependent Raman shift positions and full width at half maximum (FWHM) of the E^1_{2g} and A_{1g} vibrational modes in Yb^{3+}-doped MoS_2 thin films (240 s deposition). With increasing temperature (20 °C to 200 °C), a gradual red shift is observed in both modes, along with variations in peak broadening.

	E^1_{2g} (cm^{-1})		A_{1g} (cm^{-1})	
Temp (°C)	Position	FWHM	Position	FWHM
20	380.9 ± 0.3	9.16 ± 0.3	410.2 ± 0.3	6.9 ± 0.3
30	380.4 ± 0.2	8.46 ± 0.4	409.8 ± 0.1	6.8 ± 0.2
50	380.2 ± 0.4	8.55 ± 0.6	409.4 ± 0.2	7.1 ± 0.4
70	380.0 ± 0.5	8.60 ± 0.3	409.1 ± 0.4	6.7 ± 0.5
90	379.8 ± 0.1	8.29 ± 0.3	409.0 ± 0.3	6.8 ± 0.3
110	379.5 ± 0.3	8.36 ± 0.4	408.6 ± 0.4	6.8 ± 0.4
130	378.9 ± 0.2	8.74 ± 0.3	408.3 ± 0.2	7.0 ± 0.6
150	379.0 ± 0.4	8.26 ± 0.5	408.3 ± 0.3	6.9 ± 0.4
170	378.9 ± 0.3	8.59 ± 0.3	407.9 ± 0.1	7.1 ± 0.3
200	377.9 ± 0.2	9.16 ± 0.4	407.6 ± 0. 2	7.3 ± 0.3

3.7. Temperature-dependent Raman analysis and defect quantification

Temperature dependent Raman spectroscopy (20 °C–200 °C) was utilized to investigate the vibrational properties of Yb^{3+}-doped MoS_2 film (240 s deposition). Temperature-dependent Raman study was conducted on the 10.2 nm (240 s) MoS_2:Yb^{3+} film which is the thickest and most crystalline sample among the others in this study. This case was picked as a good example to get high signal-to-noise ratios and to develop a strong method for getting phonon anharmonicity and thermal transport parameters. Figure 8 illustrates the Raman spectra recorded at different temperatures, demonstrating the temperature-dependent progression of phonon modes. For temperature dependent Raman measurements, it is important to use appropriate laser power because high laser powers can significantly increase the local temperature on the sample [19, 45]. This often affects the Raman spectra by broadening and shifting of the Raman peaks in addition to the possibility of damaging the sample. An increase in laser power up to 0.6 mW showed no noticeable effect on the peak position or broadening of the Raman signals. Therefore, this laser power was selected for conducting the temperature-dependent Raman experiments. Table 3 lists the temperature-dependent Raman shift positions and FWHM of the E^1_{2g} and A_{1g} vibrational modes in Yb^{3+}-doped MoS_2 thin film (240 s deposition).

The temperature was raised in increments of 20 °C from 20 °C to 170 °C to precisely monitor the linear thermal shift of the Raman modes at the lower end of the temperature scale. After this, another measurement at 200 °C was performed to give a stronger constraint for the determination of the quadratic anharmonicity coefficient (β) in the fitting model and to extend the range of temperatures measured. The consistent and monotonic red shift that was seen up to 170 °C demonstrated that the phonon softening effect was already well-established and therefore the larger final step to a higher temperature

Table 4. Temperature coefficients between MoS_2:Yb^{3+}.

Mode	α ($cm^{-1}/°C$)	β ($cm^{-1}°C^2$)
E^1_{2g}	-0.0128 ± 0.0005	$(-8.7 \pm 1.7) \times 10^{-6}$
A_{1g}	-0.0186 ± 0.0005	$(+29.2 \pm 5.8) \times 10^{-6}$

without an intermediate measurement at 190 °C was justified. This strategy allowed a wide temperature range for strong fitting while at the same time, reducing the possibility of laser-induced heating effects due to longer measurement times. A validation check indicated that the values of the linear coefficient (α) fitted were consistent within the margins of errors not depending on the inclusion of the 200 °C data point and thus strengthened the reliability of the method.

The temperature evolution of Raman modes was modeled using the empirical relation (1) [$\omega(T) = \omega_0 + \alpha\ (T–T_0) + \beta\ (T–T_0)^{\ 2}$] with $T_0 = 20$ °C [18, 46]. The temperature coefficients α and β in table 4 were obtained by nonlinear least-squares fitting of the experimental Raman shifts to the empirical relation equation (1). The complete fitting of the dataset is provided in supplementary figure S11. The value of $R^2 \sim 0.98$ for both modes validates the obtained parameters. The coefficients α (linear) and β (quadratic) quantify phonon anharmonicity (table 4). The uncertainties reported for α and β in table 4 are the standard errors obtained from the covariance matrix of the fit.

For E^1_{2g}, the reduced α (-0.0128 $cm^{-1}/°C$) compared to pristine MoS_2 (-0.015 $cm^{-1}/°C$) [19, 47] indicates Yb^{3+} induced in-plane strain compensation, consistent with XPS-detected Yb_{Mo}substitution (Yb 4d peaks at 186.5 eV). The reduction in α corresponds to a Yb_{Mo} defect density of 3.2×10^{14} cm^{-2} via the relation $|\Delta\alpha/\alpha 0| = 0.47cYb$ [47] (the estimation of defect density is discussed in the supplementary section SS4). Conversely, the enhanced A_{1g} α (-0.0186 $cm^{-1}/°C$ vs. -0.014 $cm^{-1}/°C$ in pristine) reflects interlayer charge transfer, supported by Mo3*d* core-level shifts in XPS. The negligible β for E^1_{2g} (-8.7×10^{-6} $cm^{-1}/°C^2$) and positive β for A_{1g} ($+29.2 \times 10^{-6}$ $cm^{-1}/°C^2$) further confirm minimal sulphur vacancies (XPS S 2*p* at 162.3 eV shows a minor shoulder near161 eV) [48].

3.8. Thermal conductivity estimation

The in-plane thermal conductivity (κ) was approximated using Raman data via integrating phonon lifetime analysis, mean free path determination, and the kinetic theory of heat transport. The phonon lifetime (τ) was calculated from FWHM of the E^1_{2g} mode using the relation $\tau = (2\pi c\Gamma)^{-1}$, where c is the speed of light and Γ is the phonon spectral linewidth [49, 50]. At 20 °C, the measured linewidth, $\Gamma = 9.16 \pm 0.3$ cm^{-1} yields a phonon lifetime of $\tau \approx 0.58 \pm 0.02$ ps. The phonon mean free path (ℓ) was obtained via $\ell = v_s\tau$, employing the in-plane speed of sound in MoS_2, $v_s = 6.8 \times 10^3$ m s^{-1} [47, 51]. This results in $\ell \approx 3.9 \pm 0.2$ nm, indicating a reduction relative to pristine MoS_2, which exhibits $\ell \approx 5.2$ nm [47, 52]. The thermal conductivity was computed using the kinetic expression $\kappa = (1/3)C_v v_s \ell$, where the volumetric heat capacity was taken as $C_v \approx 1.5 \times 10^6$ J $(m{\cdot}K)^{-3}$ [53]. The value of κ was found to be $\approx 66 \pm 6$ W $(m{\cdot}K)^{-1}$ at 20 °C. The decrease in κ relative to pristine MoS_2 (85 W $(m{\cdot}K)^{-1}$ [19]) and few layer MoS_2 (100 W $(m.K)^{-1}$) [54] is attributed to enhanced phonon scattering introduced by trivalent Yb^{3+} dopants. The effect agrees with the observed softening in E^1_{2g} anharmonicity (temperature coefficient $\alpha = -0.0128$ $cm^{-1}/°C$ vs. -0.015 $cm^{-1}/°C$ in undoped MoS_2). The volumetric Yb_{Mo} defect density for the 10.2 nm film is $n_{Yb}{}^{3D} \approx 3.1 \times 10^{20}$ cm^{-3} (based on the areal density of 3.1×10^{14} cm^{-2}). These results are consistent with previously reported κ values decrease due to trivalent dopants such as Re in MoS_2 [55]. Yb^{3+}-doped MoS_2 allows tunable phonon transport through defect engineering to decrease in-plane thermal conductivity. This is key to miniaturized electronics, thermoelectric, and on-chip cooling technology.

In this method of thermal conductivity analysis, which is based on Raman spectroscopy, the influence of the substrate is naturally reduced to a minimum because the important factor that determines κ—the phonon lifetime (τ) is taken from the inherent linewidth of the E^1_{2g} vibrational mode. This linewidth primarily originates from phonon–phonon and phonon–defect scattering processes within the MoS_2:Yb^{3+} film rather than from interfacial effects. While substrates can impose strain or introduce minor doping, our temperature-dependent Raman measurements (table 4) show a consistent anharmonicity parameter (α) characteristic of intrinsic phonon decay in the doped MoS_2 layer. Additionally, literature reports confirm that optical phonon lifetimes obtained via Raman spectroscopy of supported 2D materials are weakly affected by substrate scattering compared to acoustic phonon transport [49–53]. The observed reduction in κ (from ~85–100 W $m{\cdot}K^{-1}$ in pristine MoS_2 to 66 ± 6 W $m{\cdot}K^{-1}$ in Yb^{3+}-doped films) is consistent with enhanced point-defect scattering from trivalent dopants [55], further supporting that the calculated κ reflects the in-plane thermal conductivity of the film. Hence the

substrate may contribute minor interfacial scattering, the dominant contribution to the measured κ is intrinsic to the MoS_2:Yb^{3+} film itself.

4. Conclusions

The present work proposes a novel predictive approach for managing the MoS_2 thin films multifunctional performance through the synergistic influence of Yb^{3+} doping and nanoscale thickness tuning. The creation of well-controlled defects at the atomic level combined with dimensional confinement leads to the very accurate tuning of the structural, optical and thermal features. Different techniques used for structural characterization such as x-ray diffraction and AFM verified the control of thickness in the range of 1–10 nm and moreover, the existence of 2 H and 1 T phases as well as that the Yb^{3+} was incorporated was disclosed by XPS measurements. The application of the Raman scattering technique led to the detection of the thickness-dependent shifts in the vibrational modes, which are indicative of the varying interlayer coupling. The introduction of Yb^{3+} ions into the MoS_2 lattice decreased the in-plane thermal conductivity ($\kappa \approx 66$ W m^{-1} K^{-1}) via the promoting the phonon scattering mechanism. The results obtained show that the defect-thickness co-engineering is a very effective and efficient design method for tailoring the electron–phonon interactions and ultimately the functional properties in MoS_2. The proposed approach could provide useful design rules for integrating doped 2D materials into optoelectronic and thermal management technologies, which can be potential for scalable device-level applications in large-scale electronics, photonics, and energy systems.

Data availability statement

The data is available upon reasonable request from the authors, as the data presented in this study is currently part of an active patent preparation process and the datasets form part of an ongoing industry collaboration.

Supplementary information available at http://doi.org/10.1088/2515-7639/ae409f/data1.

Acknowledgment

The author Geeta Sharma would like to acknowledge UKRI Grant Ref: EP/X032612/1 for providing financial support. We further thank LEMAS and Bragg's Centre, University of Leeds for providing characterization facilities. Special thanks to Zabeada Aslam and Andrew Britton for helping in carrying out HRTEM and XPS experiments.

Author contributions

Geeta Sharma 0000-0003-3392-0682
Conceptualization (lead), Data curation (lead), Formal analysis (lead), Funding acquisition (lead), Investigation (lead), Methodology (lead), Project administration (lead), Resources (lead), Validation (lead), Visualization (lead), Writing – original draft (lead), Writing – review & editing (lead)

Eric Kumi Barimah
Data curation (supporting)

Chun Wang
Data curation (supporting), Investigation (supporting)

Sarathkumar Loganathan
Data curation (supporting), Methodology (supporting)

Andrew Scott
Writing – review & editing (supporting)

Animesh Jha 0000-0003-3150-5645
Supervision (lead)

References

[1] Novoselov K S, Jiang D, Schedin F, Booth T J, Khotkevich V V, Morozov S V and Geim A K 2005 Two-dimensional atomic crystals *Proc. Natl Acad. Sci. USA* **102** 10451–3
[2] Qiu H *et al* 2024 Two-dimensional materials for future information technology: status and prospects *Sci. China Inf. Sci.* **67** 160400
[3] Lin Y C *et al* 2023 Recent advances in 2D material theory, synthesis, properties, and applications *ACS Nano* **17** 9694–747
[4] Wang Q H, Kalantar-Zadeh K, Kis A, Coleman J N and Strano M S 2012 Electronics and optoelectronics of two-dimensional transition metal dichalcogenides *Nat. Nanotechnol.* **7** 699–712
[5] Butler S Z and Goldberger J E 2013 Progress, challenges, and opportunities in two-dimensional materials beyond graphene *ACS Nano* **7** 2898–926
[6] Mak K F, Lee C, Hone J, Shan J and Heinz T F 2010 Atomically thin MoS_2: a new direct-gap semiconductor *Phys. Rev. Lett.* **105** 136805
[7] Jariwala D, Sangwan V K, Lauhon L J, Marks T J and Hersam M C 2014 Emerging device applications for semiconducting two-dimensional transition metal dichalcogenides *ACS Nano* **8** 1102–20
[8] Zhou W, Zou X, Najmaei S, Liu Z, Shi Y, Kong J, Lou J, Ajayan P M, Yakobson B I and Idrobo J C 2013 Intrinsic structural defects in monolayer molybdenum disulfide *Nano Lett.* **13** 2615–22
[9] Huang Y, Guo J, Kang Y, Ai Y and Li C M 2015 Two dimensional atomically thin MoS_2 nanosheets and their sensing applications *Nanoscale* **7** 19358–76
[10] Haldar D, Ghosh A, Ghorai U K and Saha S K 2020 Near infrared to visible upconversion photoluminescence from Er/Yb co-doped MoS_2 nanosheets with tunable thickness *Mater. Res. Bull.* **129** 110879
[11] Splendiani A, Sun L, Zhang Y, Li T, Kim J, Chim C-Y, Galli G and Wang F 2010 Emerging photoluminescence in monolayer MoS_2 *Nano Lett.* **10** 1271–5
[12] Nayyar N, Le D, Turkowski V and Rahman T S 2022 Electron-phonon interaction and ultrafast photoemission from doped monolayer MoS_2 *Phys. Chem. Chem. Phys.* **24** 25298–306
[13] Donmez Kaya M and Ozcelik S 2023 Thickness effect on electro-optical characteristics of MoS_2 /p-Si heterojunction devices fabricated by aerosol jet printing *Silicon* **15** 5513–23
[14] Pan Y, Hildebrandt P N, Zahn D, Zacharias M, Windsor Y W, Ernstorfer R, Caruso F and Seiler H 2025 Momentum-resolved signatures of carrier screening effects on electron-phonon coupling in MoS_2 *ACS Nano* **19** 11381–9
[15] Pollack E, Zhou Q, Loni E, Agbakansi K, Majed A, Wang F, Soleymani A, Busse M, Naguib M and Lu X 2025 Raman spectroscopy of 2D MoS_2 on Ti3C2 MXene: the substrate effect *Nanoscale Adv.* **7** 3456–61
[16] Ravali V and Ghosh T 2025 Electron-phonon coupling in two-dimensional Ruddlesden-Popper hybrid perovskites *Chem. Commun.* **61** 10898–910
[17] Manikandan R and Raina G 2022 *Phys. Scr.* **97** 125808
[18] Balkanski M, Wallis R F and Haro E 1983 Anharmonic effects in light scattering due to optical phonons in silicon *Phys. Rev. B* **28** 1928–34
[19] Sahoo S, Gaur A P S, Ahmadi M, Guinel M J F and Katiyar R S 2013 Temperature-dependent Raman studies and thermal conductivity of few-layer MoS_2 *J. Phys. Chem. C* **117** 9042–7
[20] Kaindl R *et al* 2017 Growth, structure and stability of sputter-deposited MoS_2 thin films *Beilstein J. Nanotechnol.* **8** 1115–26
[21] Yim C, O'Brien M, McEvoy N, Winters S, Mirza I, Lunney J G and Duesberg G S 2014 Investigation of the optical properties of MoS_2 thin films using spectroscopic ellipsometry *Appl. Phys. Lett.* **104** 103114
[22] Maddi C, Aswin J R, Scott A, Aslam Z, Willneff E, Adarsh K N V D and Jha A 2019 Structural, spectroscopic, and excitonic dynamic characterization in atomically thin Yb3+-Doped MoS_2, fabricated by femtosecond pulsed laser deposition *Adv. Opt. Mater.* **7** 1900753
[23] Sim D M, Han H J, Yim S, Choi M J, Jeon J and Jung Y S 2017 Long-term stable 2H-MoS_2 dispersion: critical role of solvent for simultaneous phase restoration and surface functionalization of liquid-exfoliated MoS_2 *ACS Omega* **2** 4678–87
[24] Hanifehpour Y, Joo S W, Hamnabard N and Jung J H 2019 The electrochemical performance and catalytic properties of Ytterbium substitution on Manganese oxide nanoparticles: BET study; preparation and characterization *J. Mater., Sci. Mater.* **30** 18897–909
[25] Chen L, Du L, Li J, Yang L, Yi Q and Zhao C 2020 Dissipative soliton generation from Yb-doped fiber laser modulated by mechanically exfoliated NbSe2 *Front. Phys.* **8** 320
[26] Fuertes V, Grégoire N, Labranche P, Gagnon S, Wang R, Ledemi Y, LaRochelle S and Messaddeq Y 2021 Engineering nanoparticle features to tune Rayleigh scattering in nanoparticles-doped optical fibers *Sci. Rep.* **11** 9116
[27] Siegel G, Venkata Subbaiah Y P, Prestgard M C and Tiwari A 2015 Growth of centimeter-scale atomically thin MoSfilms by pulsed laser deposition *APL Mater.* **3** 056103
[28] Hüser F, Olsen T and Thygesen K S 2013 How dielectric screening in two-dimensional crystals affects the convergence of excited-state calculations: monolayer MoS_2 *Phys. Rev. B* **88** 245309
[29] Gan Z X, Liu L Z, Wu H Y, Hao Y L, Shan Y, Wu X L and Chu P K 2015 Quantum confinement effects across two-dimensional planes in MoS_2 quantum dots *Appl. Phys. Lett.* **106** 233113
[30] Li H, Zhang Q, Yap C C R, Tay B K, Edwin T H T, Olivier A and Baillargeat D 2012 From bulk to monolayer MoS_2: evolution of Raman scattering *Adv. Funct. Mater.* **22** 1385–90
[31] Zhou K G, Withers F, Cao Y, Hu S, Yu G and Casiraghi C 2014 Raman modes of MoS_2 used as fingerprint of van der Waals interactions in 2-D crystal-based heterostructures *ACS Nano* **8** 9914–24
[32] Lee C, Yan H, Brus L E, Heinz T F, Hone J and Ryu S 2010 Anomalous lattice vibrations of single- and few-layer MoS_2 *ACS Nano* **4** 2695–700
[33] Maratos D M, Michail A, Stamatelatos A, Grammatikopoulos S, Anestopoulos D, Tangoulis V, Papagelis K, Parthenios J and Poulopoulos P 2024 Enhanced Raman scattering in CVD-grown MoS_2/Ag nanoparticle hybrids *Materials* **17** 4396
[34] Sledzinska M *et al* 2016 Thermal conductivity of MoS_2 polycrystalline nanomembranes *2D Mater.* **3** 035016
[35] Ferrari A C 2007 Raman spectroscopy of graphene and graphite: disorder, electron-phonon coupling, doping and nonadiabatic effects *Solid State Commun.* **143** 47–57
[36] Kuleshov N V, Lagatsky A A, Shcherbitsky V G, Mikhailov V P, Heumann E, Jensen T, Diening A and Huber G 1997 CW laser performance of Yb and Er,Yb doped tungstates *Appl. Phys. B* **64** 409–13
[37] Lu K and Dutta N K 2002 Spectroscopic properties of Yb-doped silica glass *J. Appl. Phys.* **91** 576–81
[38] He Y-M, Höfling S and Schneider C 2016 Phonon induced line broadening and population of the dark exciton in a deeply trapped localized emitter in monolayer WSe_2 *Opt. Mater. Express* **24** 8066

[39] Anon 2005 Introduction to Solid State Physics Charles Kittel
[40] Zhang Z, Ouyang Y, Cheng Y, Chen J, Li N and Zhang G 2020 Size-dependent phononic thermal transport in low-dimensional nanomaterials *Phys. Rep.* **860** 1–26
[41] Lai J M, Xie Y R and Zhang J 2021 Detection of electron-phonon coupling in two-dimensional materials by light scattering *Nano Res.* **14** 1711–33
[42] Cadiz F *et al* 2017 Excitonic linewidth approaching the homogeneous limit in MoS_2-based van der Waals heterostructures *Phys. Rev. Res.* **7** 021026
[43] Selig M, Berghäuser G, Raja A, Nagler P, Schüller C, Heinz T F, Korn T, Chernikov A, Malic E and Knorr A 2016 Excitonic linewidth and coherence lifetime in monolayer transition metal dichalcogenides *Nat. Commun.* **7** 13279
[44] Henriques J C G, Mortensen N A and Peres N M R 2021 Analytical description of the 1s exciton linewidth temperature dependence in transition metal dichalcogenides *Phys. Rev. B* **103** 235402
[45] Balandin A A 2011 Thermal properties of graphene and nanostructured carbon materials *Nat. Mater.* **10** 569–81
[46] hang Y, Fan A, Luo S, Wang H, Ma W and Zhang X 2019 Suspended 2D anisotropic materials thermal diffusivity measurements using dual-wavelength flash Raman mapping method *Int. J. Heat Mass Transfer* **145** 118795
[47] Yan R, Simpson J R, Bertolazzi S, Brivio J, Watson M, Wu X, Kis A, Luo T, Hight Walker A R and Xing H G 2014 Thermal conductivity of monolayer molybdenum disulfide obtained from temperature-dependent Raman spectroscopy *ACS Nano* **8** 986–93
[48] Peimyoo N, Shang J, Yang W, Wang Y, Cong C and Yu T 2015 Thermal conductivity determination of suspended mono- and bilayer WS2 by Raman spectroscopy *Nano Res.* **8** 1210–21
[49] Li T and Galli G 2007 Electronic properties of MoS 2 nanoparticles *J. Phys. Chem. C* **111** 16192–6
[50] Gu X and Yang R 2015 Phonon transport and thermal conductivity in two-dimensional materials *Annu. Rev. Heat Transfer* **19** 1–65
[51] Lindsay L and Broido D A 2011 Enhanced thermal conductivity and isotope effect in single-layer hexagonal boron nitride *Phys. Rev. B* **84** 155421
[52] Gu X and Yang R 2014 Phonon transport in single-layer transition metal dichalcogenides: a first-principles study *Appl. Phys. Lett.* **105** 131903
[53] Peng B, Zhang H, Shao H, Xu Y, Zhang X and Zhu H 2016 Thermal conductivity of monolayer MoS_2, MoSe2, and WS2: interplay of mass effect, interatomic bonding and anharmonicity *RSC Adv.* **6** 5767–73
[54] Majee B P, Bhawna, Singh A, Prakash R and Mishra A K 2020 Large area vertically oriented few-layer MoS_2 for efficient thermal conduction and optoelectronic applications *J. Phys. Chem. Lett.* **11** 1268–75
[55] Jenisha M A, Kavirajan S, Harish S, Kamalakannan S, Archana J, Senthil Kumar E, Wakiya N and Navaneethan M 2024 Multiple approaches of band engineering and mass fluctuation of solution-processed n-type Re-doped MoS_2 nanosheets for enhanced thermoelectric power factor *J. Colloid Interface Sci.* **653** 1150–65